

Bringing ultimate depth to scanning tunnelling microscopy: deep subsurface vision of buried nano-objects in metals

Oleg Kurnosikov*^{a, b}, Muriel Sicot^a, Emilie Gaudry^a, Danielle Pierre^a, Yuan Lu^a, Stéphane Mangin^a

Supplementary material

Validation by XPS

Figure S1 shows the XPS spectra proving the formation of subsurface nanoclusters. In principle, XPS can detect Ar embedded in solids down to 10 nm [S1]. The evolution of the $2p_{3/2}$ - $2p_{1/2}$ XPS double peak follows the processes of nanocluster nucleation and growth under annealing starting from the embedded atomic Ar. The black plot is measured just after the implantation of atomic Ar in the Cu(110) sample without any annealing. After annealing at 1050K for 5 min (the red curve) the intensity of the XPS spectra decreases indicating that a significant part of the embedded Ar has been released. The prolonged annealing at 1150K for 20 min results in the removal of almost all Ar from the sample since the blue curve shows a very faint residual trace of peak comparable to the background noise. The highest $2p_{3/2}$ peak of Ar embedded in Cu before annealing is located at 242.5 eV whereas the binding energy of the $2p_{3/2}$ peak of free gaseous Ar at high pressure is defined as 244.7 eV [S2, S3] as marked with the arrow in green (Fig. S1). The discrepancy between the binding energy of free Ar and the binding energy of Ar embedded as single atoms originates from the effect of electron screening and a

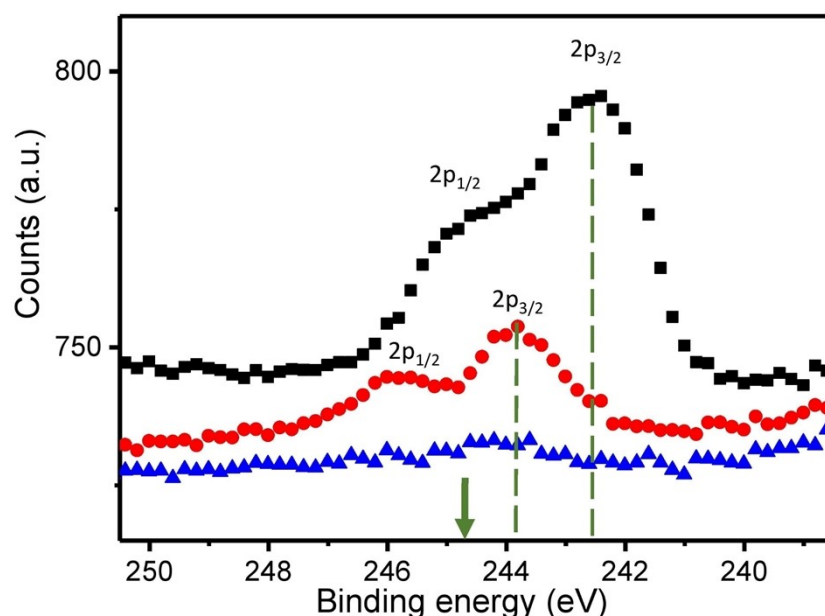


Fig. S1 XPS of Ar $2p_{3/2}$ - $2p_{1/2}$ peaks after implantation of atomic Ar in the Cu(110) sample (black), after consequent annealing at 1050K for 5 min (red), and after final annealing at 1100K for 20 min (blue).

compressed local matrix for the Ar atoms [S4 – S6]. Remarkably, after a moderate annealing, the $2p_{3/2}$ peak (the red curve) is located at 243.8 eV, i.e. shifts back towards the value expected for free Ar at high pressure. This shift can be explained by a weakening of screening due to some distance between Ar and conductive copper. The observed shift manifests that the atomic Ar agglomerates into nanoclusters.

Formation of Fe nanoclusters in Cu(001)

The subsurface Fe nanoclusters were formed in two steps: (i) deposition of less than 2 ML of Fe on Cu(001) surface with consequent annealing at 620K, and (ii) deposition of 4-96 ML of Cu in several steps with annealing at 470K. Fig. S2 shows an STM image of the sample after the initial deposition of

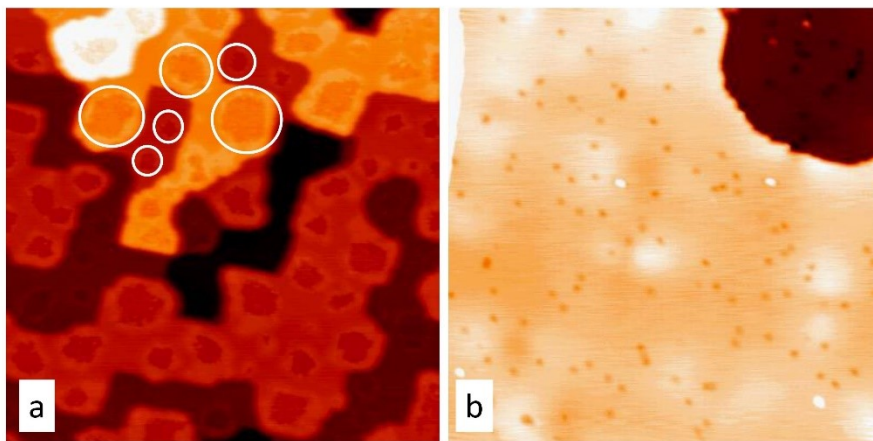


Fig. S2 STM images of the Cu(001) surface ($50 \times 50 \text{ nm}^2$) at the intermediate stage of sample fabrication: (a) – after deposition of Fe and annealing at 620K. Due to annealing, Fe forms flat nanoislands of 2 to 3 ML thick (a few of them are encircled) embedded into two or three near-surface layers of the surface. The incorporation of Fe pushes Cu towards the surface, resulting in a developed stepped structure on the surface; (b) – after capping the nanoislands with 32 ML (about 6 nm) of Cu and light annealing. A sub-atomic corrugation of the terraces appears above the buried Fe nanoislands.

of Fe and consequent annealing at 620 K. The annealing process leads to the forming flat 2-3 ML thick nano-islands of Fe embedded in the surface. The excess of Cu contributes in the terraces with a developed curling step structure. Fig.S2 (b) shows the STM image of the next step of sample fabrication. A free Cu surface shows large atomically-flat terraces with atomic impurities on them visible as dark and somewhere bright spots. Subsurface nano-islands create internal stresses resulting in some subatomic corrugation of the atomic plane, visible as chaotic patches of weak contrast in STM images. These images prove that Fe indeed forms subsurface nanoclusters.

Subsurface vision of Fe nanoclusters in Cu(001)

The QW-assisted subsurface vision can also be realized with metallic nanoclusters. Figure S3 presents the STS maps of $30 \times 30 \text{ nm}^2$ (a – c) and STS spectra (d – f) confirming the ability of subsurface STM characterization of Fe nanoclusters in Cu(001). Fe clusters less than 1 nm thick and with the lateral sizes in the range of 2 - 5 nm were buried below the Cu(001) surface. Figure S3 (a, b) shows the STS maps of the same sample with Fe nanoclusters randomly laterally distributed and buried all at 6 nm. Two STS images were scanned at two different biases corresponding to a local maximum and a local minimum of the oscillatory curve Fig. S3 (e) measured in the same location encircled in (a) and (b). The STS maps (Fig. S3 (c)) presents the ultimate depth of 25 nm when very weak traces of subsurface

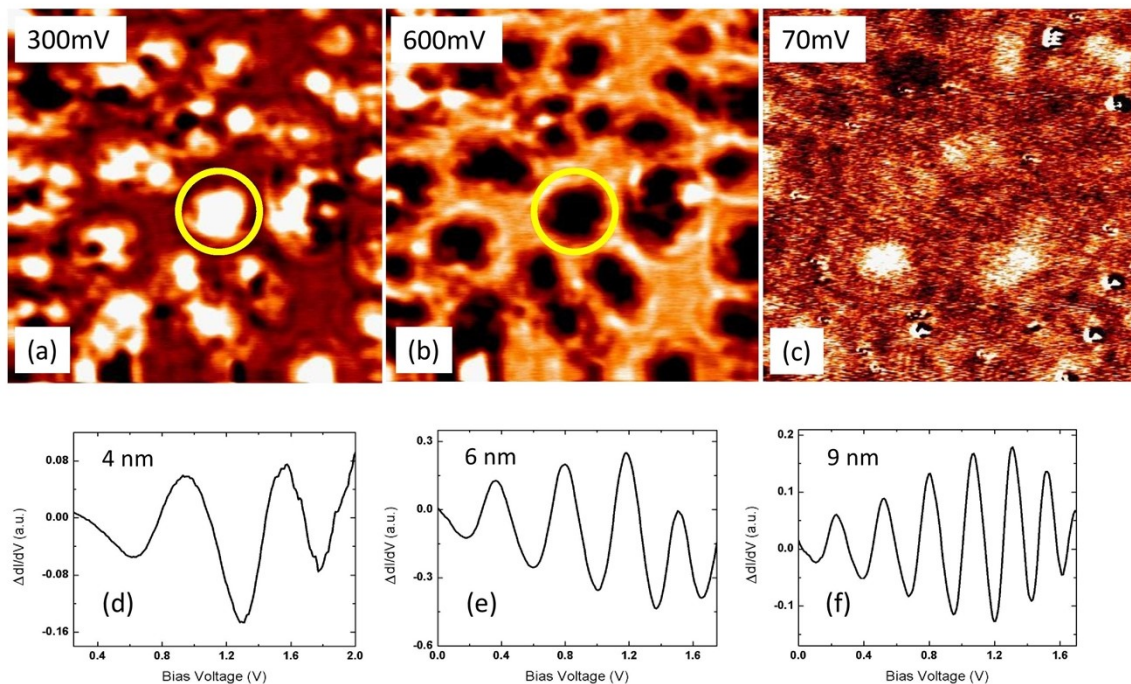


Fig. S3. (a – c) STS maps $30 \times 30 \text{ nm}^2$ of Cu(001) surface with embedded subsurface Fe nanoclusters: (a) and (b) the same sample with nanoclusters buried 6 nm below the surface and scanned with two different bias voltages; (c) STS maps of the sample with Fe nanoclusters buried at 25 nm. (d – f) Examples of oscillating conductance measured with the samples with Fe nanoclusters embedded at depths: (d) – 4 nm, (e) – 6 nm, and (f) – 9 nm. The encircled spot on (a) and (b) indicates the location where the plot (e) has been measured.

nanoclusters can be recognized. This value of the ultimate depth is defined for the temperature of 77 K at which the measurements have been performed. Note that the electronic states in the $\langle 001 \rangle$ direction do not provide focusing, therefore the ultimate depth is expected to be lower than for the Cu(110) sample. Additionally, the Fe nanoclusters reflect back only a part of electrons, therefore the intensity of reflected signal should also be weaker.

Subsurface STM sensing of interface in Fe(001)/MgO(001) epitaxial structure

The same approach can be used for characterization of interfaces in multi-layered epitaxial structure. Figure S4 (a) shows a $400 \times 400 \text{ nm}^2$ STM image of Fe(001) epitaxial layer on MgO layer after removing capping protection and slight annealing. STS measurements on flat terraces show oscillatory surface conductance in many locations of wide areas (Fig. S4 (b)). This is the result of forming QW states due to confinement between the surface and interface. The oscillation period in each location can be slightly different. This can be explained assuming the stepped structure of interface and surface. The depth of local interface can be calculated from the oscillation period that gives the depth of 2 nm for the black and blue curves and 2.4 nm for the red one. The difference in the depths corresponds to roughly 3 ML of Fe. The blue and black curves are shifted that may indicate the difference of reflection

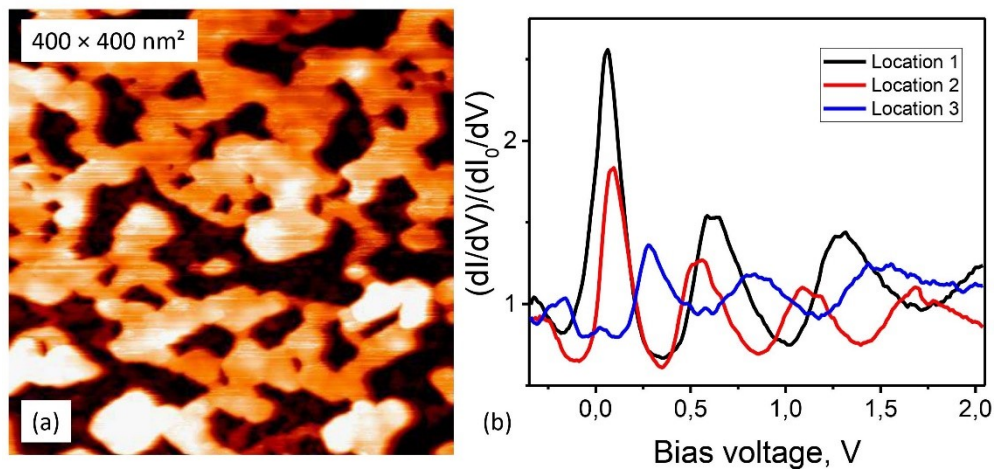


Fig. S4. (a) – STM image of Fe(001) epitaxial layer ; (b) – Normalized surface conductance in three different locations of the sample showing the oscillatory behaviour due to QW states.

conditions at the interface due to variation its structure.

Subsurface STM sensing of interface at Bi/Fe(001) structure

Subsurface sensing of interface also is demonstrated with Bi nanoislands deposited on Fe(001) surface. Figure S5 (a) presents STM image of Bi nanoisland and zoomed image of its flat upper surface (Fig. S5 (b)). Fig. S5 (c) shows a cross-section of the nanoisland of the total height of about 3 nm. Correspondingly, the STS measurements reveal peaks in LDOS (Fig. S5 (d)) originating from QW states formed between the upper flat surface of the nanoisland and the Bi/Fe interface.

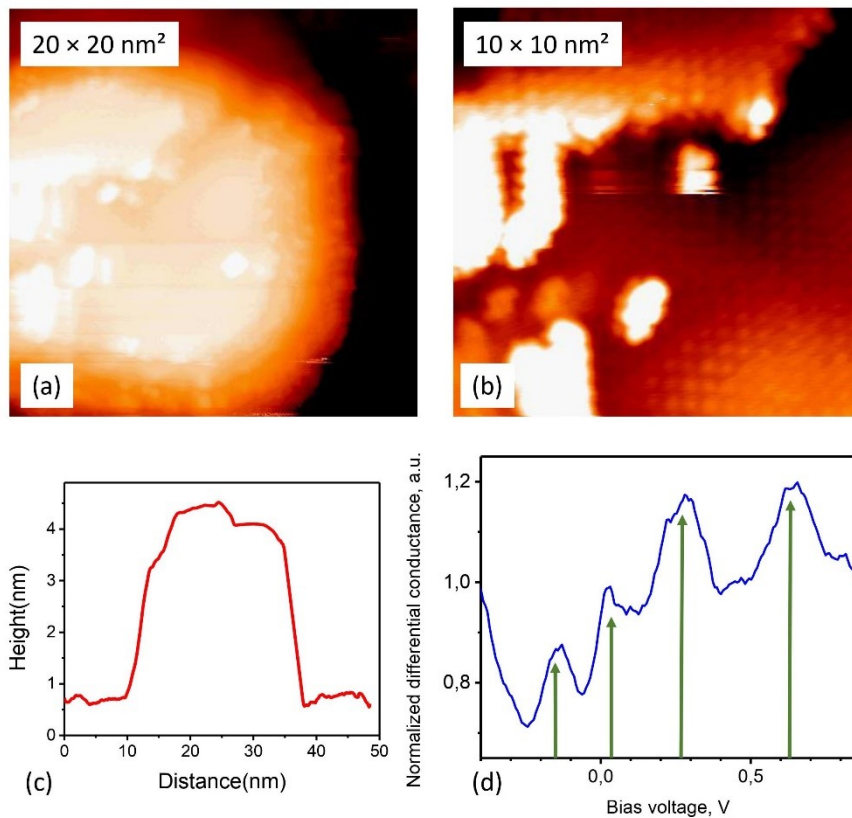


Fig. S5. (a) – STM image of Bi nanoisland on the Fe(001) surface; (b) – STM image of the surface on the top of Bi nanoisland; (c) – Cross-section of Bi nanoisland on the top of Bi nanoisland ; (d) – Normalized surface conductance with the oscillations induced by QW states.

References

- [S1] J.F. Moulder, W.F. Stickle, P.E. Sobol, K.D. Bomben, Handbook of X-ray Photoelectron Spectroscopy, Perkin-Elmer Corp, Eden Prairie, MN, 1992.
- [S2] D.I. Patel, S. Bahr, P. Dietrich, M. Meyer, A. Thissen, and M.R. Linford, Surf. Sci. Spectra 26, 014024 (2019);
- [S3] E. Tsunemi, Y. Watanabe, H. Oji, Y.-T. Cui, J.-Y. Son, and A. Nakajima, J. Appl. Phys. 117, 234902 (2015)
- [S4] Y. Baba, H. Yamamoto, and T.A. Sasaki, Surf. Sci. **287**, 806 (1993)
- [S5] M. Prenzel, T. de los Arcos, A. Kortmann, J. Winter, and A. von Keudell, J. Appl. Phys. 112, 103306 (2012)
- [S6] S. Axnanda, M. Scheele, E. Crumlin, B. Mao, R. Chang, S. Rani, M. Faiz, S. Wang, A.P. Alivisatos, and Z. Liu, Nano Lett. 2013, 13, 6176